Direct X-ray and electron-beam lithography of halogenated zeolitic imidazolate frameworks

Min Tu, Benzheng Xia, Dmitry Kravchenko, Max Lutz Tietze, Ivo Stassen, Alexander John Cruz, Tom Hauffman, Joan Teyssandier, Steven De Feyter, Zheng Wang, Roland A. Fischer, Benedetta Marmiroli, Heinz Amenitsch, Ana Torvisco Gomez, Miriam Velásquez, Paolo Falcaro, Rob Ameloot*

M. Tu, B. Xia, D. Kravchenko, M. L. Tietze, I. Stassen, A. J. Cruz and R. Ameloot

Centre for Membrane Separations, Adsorption, Catalysis, and Spectroscopy for Sustainable Solutions, KU Leuven - University of Leuven, Celestijnenlaan 200F, 3001 Leuven, Belgium

Email: rob.ameloot@kuleuven.be

A. J. Cruz and T. Hauffman

Research Group of Electrochemical and Surface Engineering, Vrije Universiteit Brussel, Pleinlaan 2, 1050 Brussels, Belgium

J. Teyssandier and S. De Feyter

Division of Molecular Imaging and Photonics, Department of Chemistry, KU Leuven - University of Leuven, Celestijnenlaan 200F, 3001 Leuven, Belgium

Z. Wang and R. A. Fischer

Catalysis Research Centre, Technical University of Munich, Garching 85748, Germany

B. Marmiroli, H. Amenitsch and A. Torvisco Gomez

Institute of Inorganic Chemistry, Graz University of Technology, Stremayrgasse 9/IV, 8010 Graz, Austria

M. Velásquez and P. Falcaro

Institute of Physical and Theoretical Chemistry, Graz University of Technology, Stremayrgasse 9/IV, 8010 Graz, Austria

Abstract

Integrating metal-organic frameworks (MOFs) in microelectronics has disruptive potential because of the unique properties of these microporous crystalline materials. Nanoscale patterning is a fundamental step in the implementation of MOFs in miniaturised solid-state devices. Conventional MOF patterning methods suffer from a low resolution and poorly defined pattern edges. Here, we demonstrate for the first time resist-free, direct X-ray and e-beam lithography of MOFs. This process avoids etching damage and contamination, and leaves the porosity and crystallinity of the patterned MOFs intact. The resulting high-quality patterns have a record sub-50 nm resolution, far beyond the state of the art in MOF patterning and approaching the mesopore regime. The excellent compatibility of X-ray and e-beam lithography with existing microfabrication processes, both in research and production facilities, provides an avenue to explore the integration of MOFs in microelectronics further. This approach is the first example of direct lithography of any type of microporous crystalline network solid, and marks an important milestone in the processing of such materials.

Main

To structure matter at the (sub-)nanometre scale, both bottom-up and top-down strategies are pursued. Bottom-up approaches, inspired by biological systems, seek to have molecular building blocks self-assemble into the desired arrangement. However, precise control over the localisation of the self-assembly sites is a challenging task. In contrast, top-down approaches use external stimuli to remove the undesired part of a larger area to create the desired shapes in the preferred location. The convergence of self-assembly and top-down approaches would lead to multiscale control over the organisation of matter, from arranging molecular building blocks to shaping the materials they form.[1–4] For instance, high-resolution patterning can be achieved by using lithographically defined guiding patterns to direct the self-assembly of engineered block copolymers.[5] In this case, self-assembly serves solely to achieve smaller-pitch patterns since the block copolymer is sacrificed. An anticipated next step in bringing together bottom-up and top-down approaches is the patterning and integration of self-assembled materials with desired properties as functional components.

Metal-organic frameworks (MOFs) are crystalline nanoporous materials that form through the self-assembly of metal ion nodes and multitopic organic linkers.[6,7] Because of their porous, crystalline, and modular nature, MOFs offer unique prospects in microelectronics and related applications, including displays, photovoltaics, low-k dielectrics and chemical sensors.[8–15] Thin film deposition and patterning are the fundamental steps to integrate any novel material in a device. However, patterning techniques for MOFs are still in their infancy, and suffer from a low resolution and poorly defined pattern edges (Supporting Information Section 1).[15–18] In conventional lithography, the pattern generated in a resist layer is etched into a film of the material of interest, followed by stripping the resist mask.[19] The few reported examples of lithographic MOF patterning follow this approach.[20–23] Direct, resist-free lithography of functional materials is desirable to minimise the number of process steps and possible contamination sources, especially for highly porous materials.[24–26] For instance, direct patterning of low-k dielectrics could eliminate resist contamination and the exposure to damaging plasma.[26–28] Herein, we report for the first time the resist-free lithography of MOFs at the micro- and nanoscale by X-ray and e-beam lithography (XRL and EBL, respectively; Figure 1). This straightforward approach enables high-quality MOF patterns in which all desirable material properties are maintained. A sub-50 nm resolution is demonstrated, which is two orders of magnitude improvement over previous lithographic MOF patterns.[20–23]

In XRL, a mask is used to pattern an X-ray-sensitive layer with a resolution down to 100 nm.[29] In contrast, EBL is a mask-less technique based on direct writing in an e-beam-sensitive material, with a resolution down to sub-10 nm.[30,31] In both techniques, the solubility of the irradiated layer changes, which enables selective dissolution of either the exposed or non-exposed region during the developing step. To evaluate the feasibility of direct lithography of MOFs, we screened the X-ray sensitivity of a variety of zeolitic imidazolate frameworks (ZIFs,[32,33] a subclass of MOFs) by exposing ZIF powders to X-rays (2-30 keV; Supporting Information Section 2). All halogenated ZIFs exhibited a clear solubility switch from a threshold dose onwards, regardless of their topology or structural metal ion. The studied halogenated ZIFs include ZIF-71, ZIF-71_Co, ZIF-72, ZIF-8_dcIm, ZIF-8_Cl and ZIF-8_Br (Figure 1a). While the pristine halogenated ZIFs are entirely insoluble in dimethyl sulfoxide (DMSO), they readily dissolved in this solvent after X-ray irradiation. In contrast, non-halogenated ZIFs did not show solubility changes in any common solvent, although the collapse of the crystalline structure occurred at high X-ray doses, in consistent with the previous report.[34]

To further evaluate halogenated ZIFs as positive-tone materials in direct lithography, films were grown through chemical vapour deposition (CVD). The two-step MOF-CVD process consists of depositing a ZnO precursor layer and subsequently converting it to the desired ZIF in an imidazole linker atmosphere.[21,35] The ZIF films were characterised by grazing-incidence small-angle X-ray scattering (GISAXS), scanning electron microscopy (SEM), atomic force microscopy (AFM) and ellipsometry (Supporting Information Section 3). To evaluate the lithographic process, an XRL mask with dots and holes of different shapes and dimensions was used (ranging from 10 to 150 µm; Figure S1). Taking 300 nm ZIF-71 films as an illustration case, the optimal volume dose was found to be 60 kJ cm^{-3}. The crystal structure of non-irradiated ZIF-71 was maintained throughout the XRL process, as confirmed by GISAXS (Figure 2a). Through the removal of the irradiated areas, even the smallest features of the mask are replicated with high fidelity in the ZIF-71 layer (Figure 2b). Profilometry together with energy-dispersive X-ray spectroscopy (EDX) mapping suggest that the irradiated area was completely removed, as further confirmed by AFM (Figure 2c, d). Furthermore, both SEM and AFM demonstrate the sharp edges of the ZIF-71 pattern (Figure 2d and S28). Besides ZIF-71, the same XRL protocol can be employed for the direct patterning of other halogenated ZIF films, with similar optimal exposure doses (60-100 kJ cm^{-3}; Supporting Information Section 4).

XRL is capable of patterning thick layers (up to mm), due to the deep penetration of the high-energy X-rays.[36] To leverage this capability, XRL was performed on 50-200 µm ZIF-8_dcIm single crystals. Positive and negative hexagonal grid masks enabled to cleanly slice through the entire crystal, in a 'cookie cutter' fashion, to yield crystals with hexagonal holes and freestanding hexagonal rods, respectively (Figure 2e, f and S46). To validate the retention of the single-crystalline nature of these particles, single-crystal X-ray diffraction was conducted. The starting ZIF-8_dclm crystallizes in the cubic Im-3m space group.[37] Remarkably, the diffraction patterns of the single crystals after XRL were of high enough quality to determine the unit cell parameters as identical to those of the starting crystals (Table S3), thus demonstrating that XRL maintains the single-crystalline nature. This patterning approach could enable hierarchical structures with highly ordered porosity at multiple length scales, which are of interest in a range of applications.[38–40]

To leverage MOFs in solid-state devices, patterning should not alter their desirable properties, especially their porosity. Notably, such tests have not been considered previously.[15,16] The porosity of patterned ZIF-71 films was studied by krypton (Kr) and methanol physisorption on MOF-coated micropillar arrays and quartz crystal microbalance (QCM) substrates, respectively (Figure 3a-d). The MOF-CVD process enables conformal ZIF-71 coatings on the pillar arrays, resulting in a geometric surface area enhancement that enables Kr sorption measurements (Figure S29).[21] The resulting type I isotherm and the Brunauer-Emmett-Teller (BET) surface area per film area of 247 m^2 m^{-2} demonstrate the microporous nature of the ZIF-71 coating before X-ray irradiation (Figure 3c). Based on the calculated ZIF-71 density (1.17 g cm^{-3}) and measured film thickness (200 nm), a specific BET surface area of 1055 m^2 g^{-1} is found, similar to values reported for powder samples.[41] After X-ray irradiation and removal of the coating on half of the pillar array, the BET surface area of the remaining ZIF-71 film was virtually unchanged (236 m^2 m^{-2}; Figure 3c). Gravimetric QCM monitoring shows an S-shaped methanol adsorption isotherm (Figure 3d), in good agreement with data reported for ZIF-71 powder samples.[42] By using the removed film fraction as a correction factor, the gravimetric methanol isotherms of the patterned and unpatterned ZIF-71 films overlap. These results illustrate the remaining ZIF-71 film after XRL fully retains its porosity.

Due to their periodicity, the ZIF-71 patterns formed by XRL are efficient diffraction gratings for light in the visible range (Figure 3e, f).[43] Taking advantage of the MOF's porosity, a ZIF-71 pattern on a transparent substrate was used as a diffraction grating vapour sensor (Figure 3g). When guest molecules adsorb in the pores, the phase difference resulting from the ZIF-71 pattern increases together with the refractive index of the MOF layer. Therefore, guest adsorption can be transduced through monitoring the intensity changes of the first-order diffraction spots.[43] This principle was illustrated for methanol vapour sensing using a 200 nm thick ZIF-71 diffraction grating covering a 4×4 mm^2 area (Figure 3g, h). The resulting sensing data are in excellent agreement with the *in situ* ellipsometry and QCM reference adsorption experiments. Despite its simplicity, this example illustrates the potential of scalable high-resolution patterning of MOF films.

The initially white halogenated ZIF powders turn brown upon X-ray exposure (Figure S6), indicating a chemical change of the imidazolate linkers. X-ray-induced changes typically comprise primary and secondary phenomena. Primary bond breaking occurs because of the interaction between the X-rays and the irradiated material through photoelectric, Compton or Auger effects.[34,44] Secondary reactions are the result of radiolytic products such as free radicals generated by the energetic electrons.[45,46] Since halogenated ZIFs undergo both decomposition and a solubility switch, while non-halogenated ZIFs only exhibit amorphisation (Supporting Information Section 2), halogen atoms on the structural linkers evidently play a vital role in these processes. GISAXS data show that ZIF-71 films become amorphous at X-ray doses over 10 kJ cm^{-3}, while a dose higher than 60 kJ cm^{-3} is required for a complete solubility switch (Figure 4a). This result suggests that low X-ray doses induce the amorphisation because of primary damage, and further reactions take place at higher doses. While the solution ^{1}H nuclear magnetic resonance (NMR) spectrum of the pristine dcIm linker has only one peak at ~7.5 ppm, a large number of peaks appear in the 6.5-9 ppm and 2.5-1.5 ppm ranges after X-ray irradiation (Figure 4b). The peaks indicate bond cleavage of imidazolate ring and the formation of different imines, C-H bonds or amines. These chemical changes are likely catalysed by Cl radicals that are sufficiently reactive to initiate C-H activation, C-C bond cleavage, and ring-opening reactions.[47–50]

The X-ray-induced changes of ZIF-71 films were studied by X-ray photoelectron spectroscopy (XPS). No obvious changes were found in the Zn 2P spectra, indicating no reduction of Zn^{2+} (Figure S47). In the N 1S XPS spectra, both C-N and Zn-N peaks decrease along with an increase of the N-H signal, suggesting cleavage of the imidazole ring C-N bonds and the framework Zn-N bonds (Figure 4e, f). The decrease of C-Cl signal together with the rise of the Zn-Cl signal suggests the formation of Cl radicals by the homolysis of C-Cl bonds (Figure 4d, f). These Cl radicals likely initiate the cleavage of C-C, C-N, and Zn-N bonds, resulting in further reactions between the formed fragments. No change in composition is observed (Table S4), suggesting that negligible material is lost through volatilisation during X-ray exposure. Figure 4c displays the elemental analysis of the water-soluble and -insoluble fractions of X-ray irradiated ZIF-71. Both fractions contain C, N, and Cl, while only the water-soluble fraction contains Zn. Therefore, the X-ray-induced breakdown of the dcIm linker seems to result in an at least partially polymerised organic fraction and a water-soluble fraction consisting of Zn-Cl salts, and Zn-N or Cl-Zn-N complexes. In contrast, the imidazolate linkers of non-halogenated ZIFs remain intact upon X-ray induced amorphisation.[34] Therefore, the crucial role of the halogen atoms is to catalyse the imidazolate ring fragmentation upon X-ray exposure, thus enabling dissolution and direct lithography.

XRL resists can commonly also be applied in EBL, since the electron beam has the same effect as the photoelectrons generated by X-rays.[31,51] It was previously observed that repeated scanning during

electron microscopy can induce amorphisation of non-halogenated ZIFs, resulting in a less soluble amorphous deposit.[52] Analogous to the different behaviour of non-halogenated and halogenated ZIFs in XRL, the latter behave as positive-tone materials in direct EBL. The optimal e-beam area dose for ZIF-71 patterning was found to be ~1000 µC/cm^2 (Supporting Information Section 6). The irradiated part cannot be developed completely at lower irradiation doses, while higher doses resulted in a mismatch between the developed and exposed areas due to scattering of the primary, secondary and backscattered electrons.[53–55] Patterns with different shapes and feature sizes were obtained by direct e-beam writing in a 100 nm thick ZIF-71 film and subsequent development in DMSO. Straight lines with sharp edges were achieved for features down to 50 nm (Figure 5a-d and S57). In all patterns, the ZIF-71 crystal facets remain clearly visible, suggesting that the patterned MOF remained intact, as during XRL. AFM data (Figure 5b) suggests that most of the irradiated area was developed, except for a small residue that probably formed by e-beam-induced cross-linking of linker fragments. High-resolution patterning with features below 50 nm can be realized, although the pattern edge quality deteriorates because of proximity effects (Figure 5e, f and S58). Higher resolution may be achievable by systematic optimisation of patterning parameters such as beam energy, beam current, field parameters and deflection mode.[56]

Conclusion

In summary, we demonstrated for the first time the direct lithographic patterning of MOFs, without the use of resist layers. This approach is the first example of direct lithography of any type of microporous crystalline network solid, and marks an important milestone in the processing of such materials. The resulting patterns have a high uniformity and edge quality, with a record sub-50 nm resolution, far beyond the state of the art in MOF patterning and approaching the mesopore regime. The crystallinity and porosity of the patterned MOF films is maintained. The excellent compatibility of XRL and EBL with established microfabrication processes will considerably expedite the integration of MOF materials in microelectronics and related applications requiring, for example, state-of-the-art low dielectric constant, low refractive index or low density/high surface area materials.
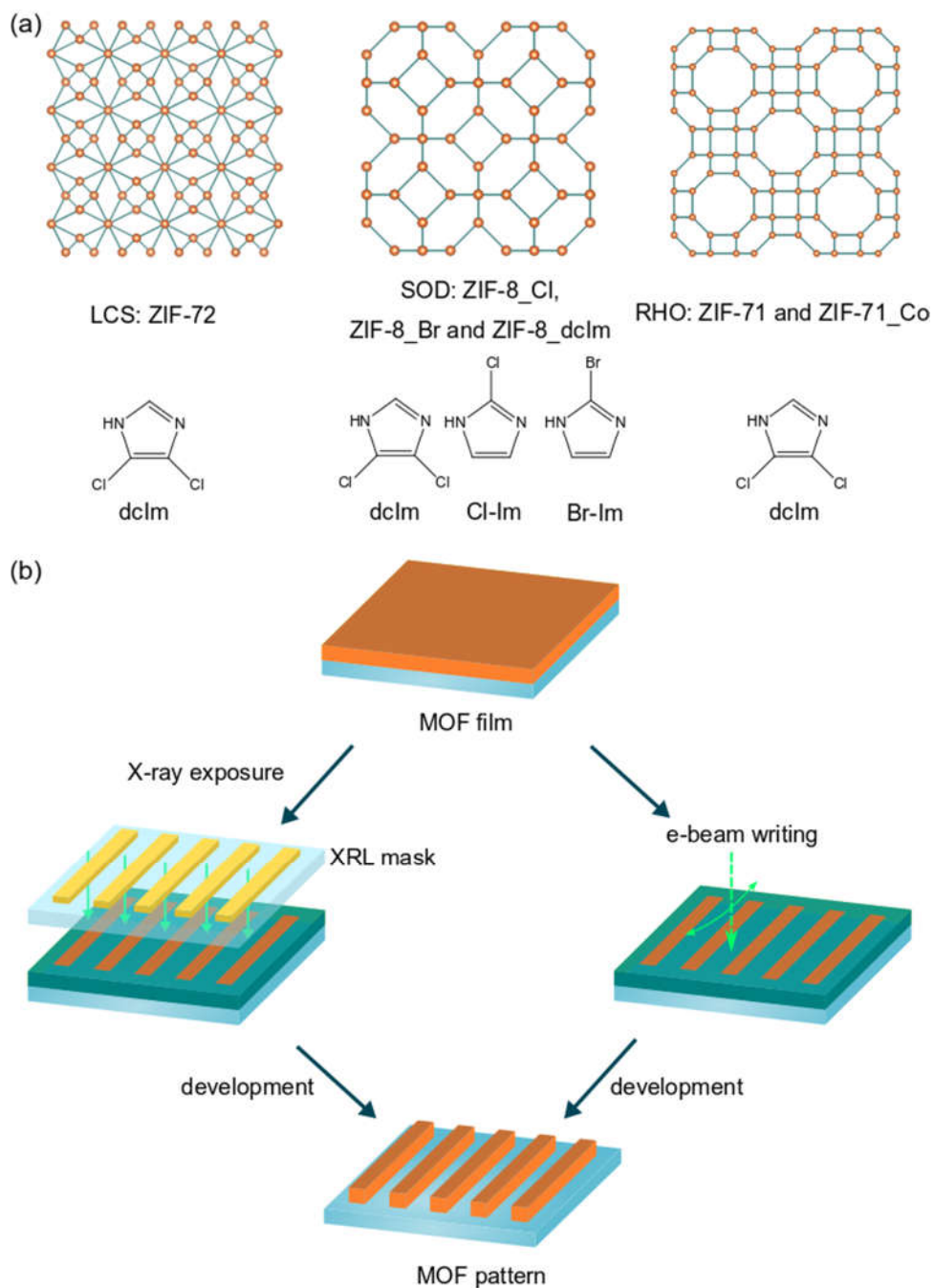
Figure 1. Direct patterning of MOF films by XRL and EBL. (a) Ball-and-stick representation of halogenated ZIFs that can be directly patterned by XRL and EBL. Capitalised three-letter codes are used to describe ZIF topologies. Cl-Im, Br-Im and dcIm represent the linkers of 2-chloroimidazole, 2-bromoimidazole and 4,5-dichloroimidazole, respectively. All ZIFs are Zn based except ZIF-71_Co. (b) Schematic illustration of direct top-down patterning of MOF films by XRL and EBL.
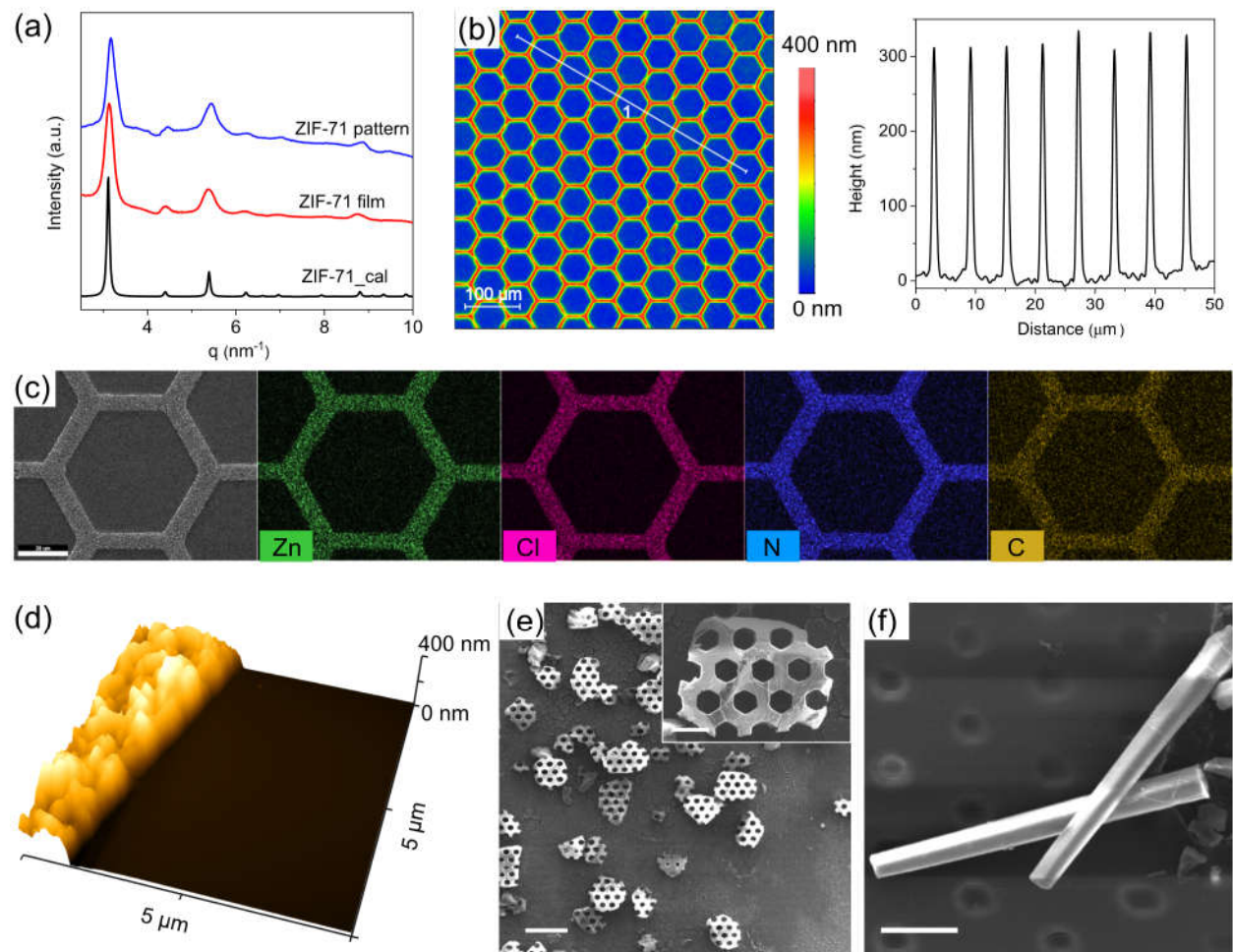
Figure 2. Characterisation of halogenated ZIFs after XRL patterning. (a) Synchrotron GISAXS patterns of 300 nm thick ZIF-71 films before and after XRL, in comparison with the calculated ZIF-71 PXRD pattern. (b) Optical profilometry of the patterned ZIF-71 film and the line profile extracted from this image. (c) SEM-EDX mapping (Zn, Cl, N and C) of the patterned ZIF-71 film. (d) AFM image of the edge of the ZIF-71 pattern. (e-f) SEM images of ~100 μm ZIF-8_dcIm single crystals after XRL patterning with a positive and negative hexagonal grid mask, respectively. The resulting particles retain their single-crystalline nature. Scale bars: (b) 100 μm; (c) 20 μm; (e) 200 μm and 50 μm for inset; (f) 20 μm.
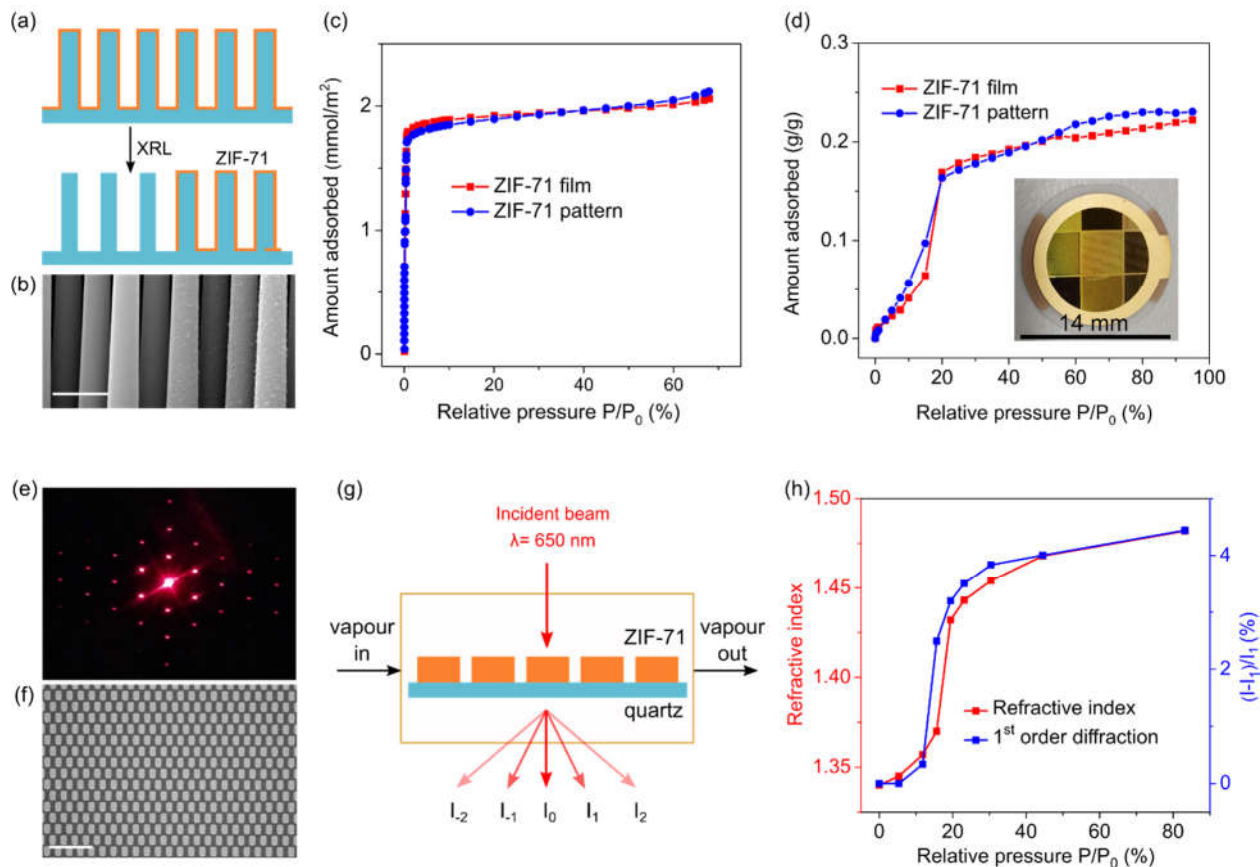
Figure 3. Porosity characterisation and sensing application of patterned ZIF-71 films. (a) Scheme of XRL patterning of a ZIF-71-coated Si pillar array for Kr physisorption. (b) Cross-section SEM image of a Si pillar array after removal of the ZIF-71 film in the left half. Scale bar: 5 µm. (c) Kr adsorption isotherms of ZIF-71-coated Si pillar arrays before and after XRL. The uptake values, per square metre of MOF, are plotted by only considering the MOF-covered area for the patterned pillar array. (d) Methanol adsorption isotherms of ZIF-71-coated QCM substrates before and after XRL. Specific uptake values, per gram of MOF, are plotted by only taking the MOF-covered area into account for the patterned film. Inset: photograph of the ZIF-71 pattern on a QCM substrate. Each of the squares consists of different geometries. (e) Picture of the diffraction pattern resulting from illuminating a ZIF-71 pattern on quartz with a red laser pointer. (f) Optical microscopy image of the corresponding patterned ZIF-71 film acting as a diffraction grating. Scale bar: 100 µm. (g) Scheme of the evaluation of ZIF-71 patterns as diffraction grating vapour sensors. (h) Evolution of the refractive index of a ZIF-71 film measured by ellipsometry (red) and the normalized intensity of the 1st order diffraction spot (I_1) of the ZIF-71 grating (blue) as a function of methanol vapour pressure.
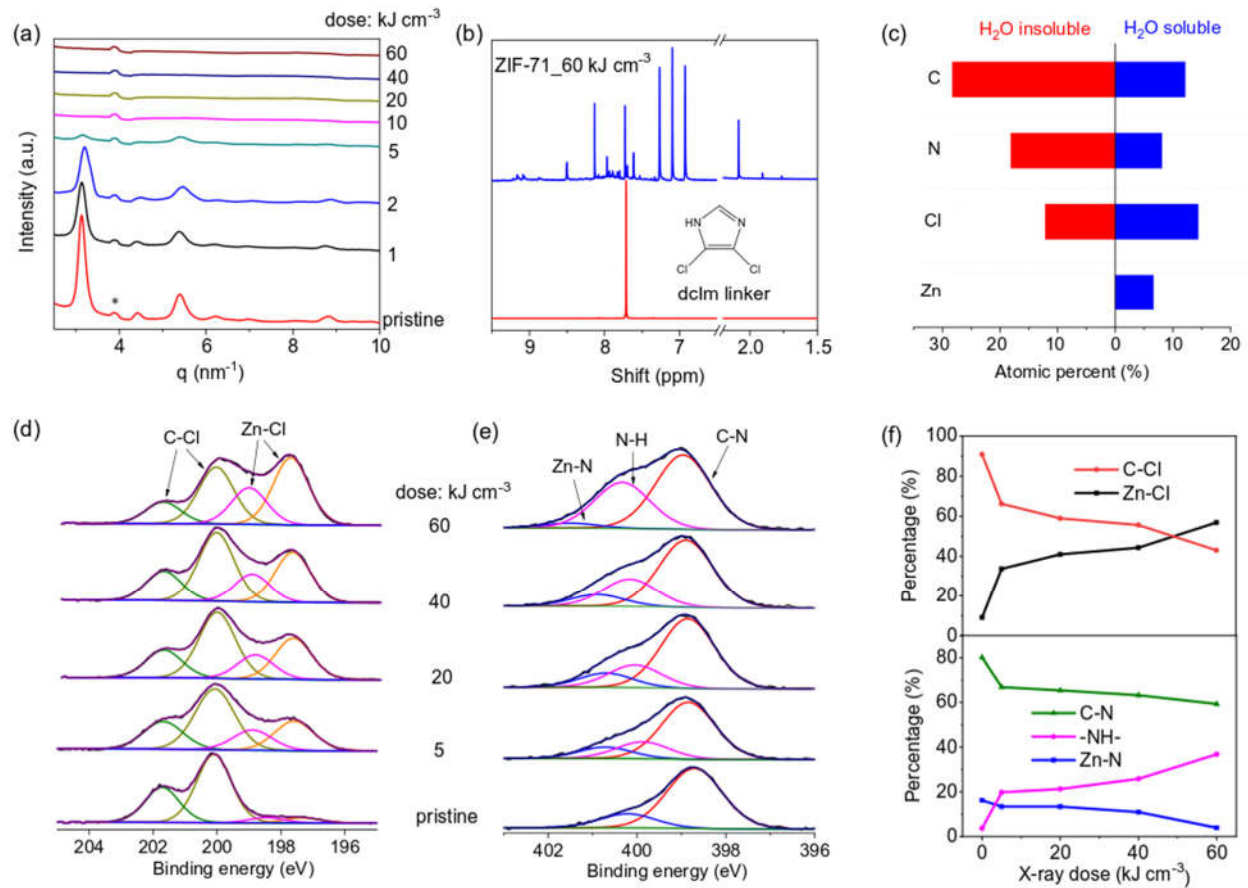
Figure 4. Mechanistic investigation of the X-ray dose effect on ZIF-71. (a) *Ex situ* synchrotron GISAXS patterns of a ZIF-71 film as a function of X-ray dose. The asterisk represents a detector artefact. (b) Solution ^{1}H NMR spectra of dcIm linker (red) and X-ray irradiated ZIF-71 powder (60 kJ cm^{-3}, blue) in DMSO_d6. (c) Elemental analysis of the water-soluble and -insoluble fractions of ZIF-71 powder after X-ray exposure (60 kJ cm^{-3}). XPS Cl 2p (d) and N 1s (e) spectra of a 200 nm ZIF-71 film as a function of X-ray dose. (f) The proportion of Cl bonds (C-Cl and Zn-Cl, top) and N bonds (C-N, N-H, and Zn-N, bottom) as a function of X-ray dose, calculated from the XPS spectra.
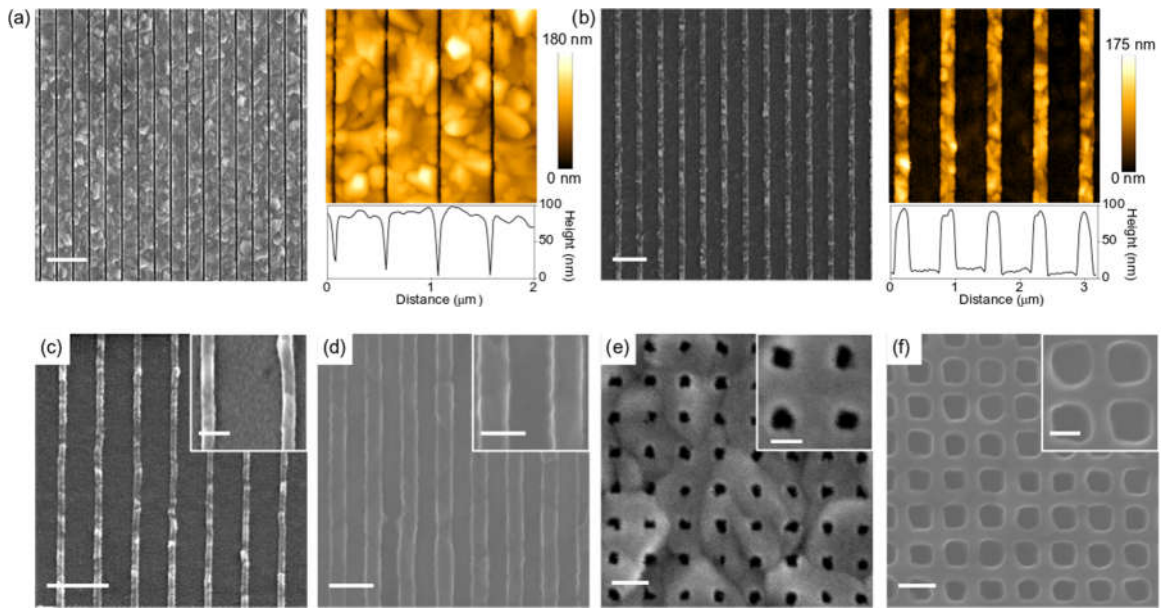
Figure 5. High-resolution EBL patterning of 100 nm thick ZIF-71 films. (a) SEM and AFM images of 50 nm trenches etched into the ZIF-71 film. (b) SEM and AFM images of 200 nm lines. (c-d) SEM images of 100 nm and 60 nm lines, respectively. (e-f) 40 nm holes and grid with a 30 nm line width etched in the ZIF-71 film. Scale bars: (a) and (b) 1 μm; (c) 1 μm and 200 nm for inset; (d) 200 nm and 100 nm for inset; (e) and (f) 100 nm and 50 nm for inset.

Methods

MOF thin film deposition

Single-side polished and back-etched Si wafers were used. Si pillar arrays with a diameter and height of 2 and 50 µm, respectively, were produced by deep reactive ion etching (Bosch process). The MOF film deposition consists of two steps: 1) ZnO precursor layer deposited by atomic layer deposition (ALD); 2) vapour solid conversion of ZnO layer in an organic linker atmosphere. The ZnO films were deposited using a Savannah S-200 thermal ALD reactor (Veeco Instruments, Inc.) with deionized water and diethylzinc as precursors. The pulse and purge durations for the ALD precursors were set to 0.015 s and 5 s, respectively. The reactor base pressure was ~ 0.4 mbar at an N_2 gas flow of 20 sccm. This process resulted in a ZnO growth rate of 1.7 Å/cycle on Si substrates at 120 °C. In the case of ZIF-71 deposition, ZnO film, 50 mg of 4,5-dichloroimidazole (dcIm) powder and a small quantity of DMF (50 µL) were placed separately in a 250 mL schlenk tube. After heating in a convection oven at 110 °C for 1 day, ZIF-71 film was obtained. ZIF-8_Cl and ZIF-8_Br were deposited by the same method using 2-chloroimidazole (Cl-Im) and 2-bromoimidazole (Br-Im), respectively. The ZIF-72 film was deposited at 150 °C without the addition of DMF. The obtained MOF films were activated by heating at 150 °C under dynamic vacuum (0.1 mbar) for 1 day.

X-ray lithography

XRL was performed at the XRL beamline of Elettra synchrotron (Trieste, Italy).[57] A scheme of the filter chamber and of the XRL scanner is shown in Figure S1. Samples can be directly exposed to the X-ray beam, or a mask containing patterns can be placed in front of the sample. The X-ray beam is composed of different energies (2-30 keV) with a characteristic wavelength of 3.22 keV. The two main setups are the one for films deposited on flat substrates and the one for holding powders. The film sample holder is the standard one available in every XRL beamline. The powder sample holder consists of a 200 µm trench machined in a stainless steel block. The patterning of ZIF-8_dcIm single crystals was performed in the film patterning mode by spreading out the crystals on double-side Kapton tape. The mask employed for the patterning of the film, contains arrays of dots and holes with different shape (squares, circles, hexagon, lines) with different dimensions (5-150 µm) and spacing (5.5-150 µm). A picture of the mask is shown in Figure S1. In XRL, the dose is commonly expressed as energy per unit volume absorbed at the bottom of the exposed material (traditionally expressed as kJ cm^{-3}). It takes into account the thickness of the material and its attenuation length (in the energy range of the X-ray beam spectrum). The typical X-ray doses for the patterning of ZIF-71, ZIF-8_Cl, ZIF-8_Br and ZIF-72 are 60, 80, 80 and 100 kJ cm^{-3}, respectively.

Electron beam lithography

The EBL of MOF films was performed on a nanofabrication system from Raith GmbH. The working distance was set to 10 mm. The typical acceleration voltage was 20 kV. The beam current, measured by a Faraday cup, was in the range of 300-350 pA. The step sizes of the area and line doses were set to 10 nC/ cm^2 and 1000 pC/cm, respectively. The patterns were written in a concentric and clockwise mode.

Small-angle X-ray scattering

SAXS data were collected on the SAXS beamline at the ELETTRA synchrotron light source (Trieste, Italy) using a photon energy of 8 keV.[58] Images were recorded using the Pilatus3 1M detector (DECTRIS Ltd., Baden-Daettwil, Switzerland). The powder samples were recorded in capillary mode. The beamline setup was adjusted to a sample-to-detector distance of 757 mm to result in an available q range between 0.1 and 9.8 nm^{-1}. In the case of GISAXS, the beamline setup was adjusted to a sample-to-detector distance of 286 mm. A secondary vertical beamstop was used to safeguard the detector, resulting in an anisotropic q range of 0.1-25 nm^{-1}. All measurements were done at an incidence angle of 0.36°. The calibration and the calculation of the vertical slices were conducted using the FIT2D software package.[59]

Single-crystal X-ray diffraction

SCXRD data was collected for pristine and patterned ZIF-8_dcIm crystals on a Bruker APEX II diffractometer with an Incoatec microfocus Mo Kα tube (λ= 0.71073 Å) and a CCD area detector. Empirical absorption corrections were applied using SADABS or TWINABS.[60] The structures were solved with the use of the intrinsic phasing option in SHELXT and refined by the full-matrix least-squares procedures in SHELXL.[61] The space group assignments and structural solutions were evaluated using PLATON.[62] Non-hydrogen atoms were refined anisotropically. Hydrogen atoms were located in calculated positions corresponding to standard bond lengths and angles and refined using a riding model. Atomic positions in the framework were evaluated by using the "squeeze" option available in the PLATON program suite.[63]

Scanning electron microscopy

SEM images were recorded using a FEI XL30FEG instrument after sputter-coating the samples with 5 nm Pt. EDX mapping was recorded by an EDAX detector with a resolution of 512 × 512 pixels.

Atomic force microscopy

AFM topography images (512 × 512 pixels) were recorded in intermittent contact mode using an Asylum Research Cypher ES AFM instrument at ambient conditions using Si cantilevers (OLYMPUS, AC160TS-R3). Data analysis was performed using Gwyddion 2.44.[64]

Optical profilometry

Optical profilometry images were recorded on a Sensofar 3D optical profilometer at ambient conditions. Data analysis was performed using Gwyddion 2.44 software.[64]

Porosity study

Both N_2 and Kr sorption isotherms were measured at 77 K using a Micromeritics 3Flex physisorption instrument. The samples were degassed before measurements at 423 K under dynamic vacuum (10^{-2} mbar) for 12 h. The BET method was applied in the region between 0.005 and 0.05 P/P_0, according to the consistency criteria for microporous materials. Methanol adsorption isotherms on ZIF-71-coated QCM substrates were measured using a BEL-QCM instrument at 298K.[65] The equilibrium time was set to 5 min.

Ellipsometry

The optical properties of the deposited layers were measured using an M-2000x spectroscopic ellipsometer (J. A. Woollam Co. Inc., λ = 246-1000 nm). A two-layer optical model was used, consisting of a native oxide layer and a MOF layer to be analysed. For MOF films, the Cauchy model was used with variable thickness and optical constants. The bare Si substrates were measured to determine the thickness of the native oxide before every experiment. The ellipsometric parameters of the Si substrate and the native oxide were taken from literature[66] and kept fixed for all measurements. *In situ* ellipsometry porosimetry measurements were performed on a custom-built tool featuring a vacuum chamber, spectroscopic ellipsometer (Sentech SE801, 350–850 nm wavelength), and a programmable adsorbate dosing platform. The isotherms were recorded at room temperature. The equilibration time at each pressure point was set to 5 min.

Diffraction grating vapour sensing

In the configuration of Figure 3g, a phase difference (φ) is created when light passes through a MOF pattern deposited on a transparent substrate (equation 1).

$$\varphi = \frac{2\pi d(n_{MOF} - n_{air})}{\lambda} \qquad (1)$$

In which φ is the phase difference, d is the MOF film thickness, n_{MOF} and n_{air} are the refractive indices of the MOF and the surrounding atmosphere, respectively, and λ is the wavelength of the incident beam.

When guest molecules are adsorbed in the MOF pores, the resulting refractive index increase of the MOF layer causes a larger phase difference. Thus, guest adsorption can be transduced through monitoring the intensity changes of the first-order diffraction spots (equation 2).[43]

$$I_1 = \frac{2(1 - \cos\varphi)}{\pi^2} \quad (2)$$

In which I_1 is the first-order diffraction intensity, and φ is phase difference of the grating.

Vapour sensing was performed by illuminating MOF patterns on quartz substrates, horizontally positioned in a sealed enclosure (Linkam stage) which is connected to a vapour generating system. A 650 nm laser (Picotronic, modulated with adjustable focus) is used as light source. The diffraction pattern are directly captured with a CMOS camera (Flir Chameleon 3, 2048x1536 pixel, monochrome, typ. grating-sensor distance ca. 10 cm). During dosing of methanol vapours, the intensity of a first-order diffraction spot was monitored every 2 s by integrating the CMOS response over 136x136 pixel around the spot (PySpin). To adjust the incoming laser intensity, PWM and a polarizer are used.

Nuclear magnetic resonance spectroscopy

Solution ^{1}H NMR spectra were recorded on a Bruker Advance 300 MHz spectrometer. DMSO-d_6 was used as a solvent to dissolve dcIm linker and X-ray irradiated ZIF-71 powder samples.

Elemental analysis

Elemental analyses for C, H and N were carried out on a Hekatech EuroEA Elemental Analyser. Zn content was determined by atomic absorption spectroscopy after decomposing the sample in a mixture of sulfuric acid and nitric acid in a microwave. Cl content was determined by potentiometric titration using an Agilent technologies 200 series AA.

X-ray Photoelectron Spectroscopy

XPS data for X-ray irradiated ZIF-71 films were collected using a PHI5600 Versaprobe II (Physical Electronics) utilizing a Al Kα monochromatic X-ray source (1486.71 eV photon energy) with a beam irradiation power of 25 W. The kinetic energy of the photoelectrons was measured with a take-off angle of 45° and a spot diameter of 100 μm to measure surface compositions up to ~5 nm in depth. The analysis and fitting were performed using CasaXPS software (Casa Software, Ltd.) employing a mixed Gaussian-Lorentzian peak shape and a Shirley-type background.

Infrared spectroscopy

Attenuated total reflection Fourier-transform infrared spectroscopy (ATR-FTIR) spectra were recorded on a Varian 670 FTIR spectrometer equipped with a VeeMAXTM III accessory (PikeTech). The spectra were collected with a Ge ATR crystal at an incidence angle of 60°. 64 scans were accumulated by either a DLaTGS or MCT detector with a resolution of 4 cm^{-1}.

Acknowledgements

with the installation of the diffraction grating sensor setup, Dr. B. Raes and Prof. J. van de Vondel for help with the EBL setup, and M. Krishtab for the discussion on MOFs for low-k dielectrics.

Competing interests

The authors declare no competing financial interests.

References

1. Liddle, J. A. & Gallatin, G. M. Nanomanufacturing: A Perspective. *ACS Nano* **10**, 2995–3014 (2016).
2. Isaacoff, B. P. & Brown, K. A. Progress in Top-Down Control of Bottom-Up Assembly. *Nano Lett.* **17**, 6508–6510 (2017).
3. Cheng, J. Y., Ross, C. A., Smith, H. I. & Thomas, E. L. Templated Self-Assembly of Block Copolymers: Top-Down Helps Bottom-Up. *Adv. Mater.* **18**, 2505–2521 (2006).
4. Smith, K. H., Tejeda-Montes, E., Poch, M. & Mata, A. Integrating top-down and self-assembly in the fabrication of peptide and protein-based biomedical materials. *Chem. Soc. Rev.* **40**, 4563–4577 (2011).
5. Liu, C.-C. *et al.* Directed self-assembly of block copolymers for 7 nanometre FinFET technology and beyond. *Nat. Electron.* **1**, 562–569 (2018).
6. Batten, S. R. *et al.* Terminology of metal-organic frameworks and coordination polymers (IUPAC Recommendations 2013). *Pure Appl. Chem.* **85**, 1715–1724 (2013).
7. Furukawa, H., Cordova, K. E., O'Keeffe, M. & Yaghi, O. M. The Chemistry and Applications of Metal-Organic Frameworks. *Science* **341**, (2013).
8. P. Lustig, W. *et al.* Metal–organic frameworks: functional luminescent and photonic materials for sensing applications. *Chem. Soc. Rev.* **46**, 3242–3285 (2017).
9. Feng, D. *et al.* Robust and conductive two-dimensional metal–organic frameworks with exceptionally high volumetric and areal capacitance. *Nat. Energy* **3**, 30–36 (2018).
10. Arora, H. *et al.* Demonstration of a Broadband Photodetector Based on a Two-Dimensional Metal–Organic Framework. *Adv. Mater.* **32**, 1907063 (2020).
11. Dong, R. *et al.* High-mobility band-like charge transport in a semiconducting two-dimensional metal–organic framework. *Nat. Mater.* **17**, 1027–1032 (2018).
12. Skorupskii, G. *et al.* Efficient and tunable one-dimensional charge transport in layered lanthanide metal–organic frameworks. *Nat. Chem.* **12**, 131–136 (2020).
13. Chueh, C.-C. *et al.* Harnessing MOF materials in photovoltaic devices: recent advances, challenges, and perspectives. *J. Mater. Chem. A* **7**, 17079–17095 (2019).
14. Krishtab, M. *et al.* Vapor-deposited zeolitic imidazolate frameworks as gap-filling ultra-low-k dielectrics. *Nat. Commun.* **10**, 1–9 (2019).
15. Stassen, I. *et al.* An updated roadmap for the integration of metal–organic frameworks with electronic devices and chemical sensors. *Chem. Soc. Rev.* **46**, 3185–3241 (2017).
16. Falcaro, P. *et al.* MOF positioning technology and device fabrication. *Chem. Soc. Rev.* **43**, 5513–5560 (2014).

17. Falcaro, P., Buso, D., Hill, A. J. & Doherty, C. M. Patterning Techniques for Metal Organic Frameworks. *Adv. Mater.* **24**, 3153–3168 (2012).

18. Allendorf, M. D., Schwartzberg, A., Stavila, V. & Talin, A. A. A Roadmap to Implementing Metal–Organic Frameworks in Electronic Devices: Challenges and Critical Directions. *Chem. Eur. J.* **17**, 11372–11388 (2011).

19. Ito, T. & Okazaki, S. Pushing the limits of lithography. *Nature* **406**, 1027–1031 (2000).

20. Lu, G., Farha, O. K., Zhang, W., Huo, F. & Hupp, J. T. Engineering ZIF-8 Thin Films for Hybrid MOF-Based Devices. *Adv. Mater.* **24**, 3970–3974 (2012).

21. Stassen, I. *et al.* Chemical vapour deposition of zeolitic imidazolate framework thin films. *Nat. Mater.* **15**, 304–310 (2016).

22. Okada, K. *et al.* Copper Conversion into Cu(OH)2 Nanotubes for Positioning Cu3(BTC)2 MOF Crystals: Controlling the Growth on Flat Plates, 3D Architectures, and as Patterns. *Adv. Funct. Mater.* **24**, 1969–1977 (2014).

23. Razmjou, A. *et al.* Preparation of Iridescent 2D Photonic Crystals by Using a Mussel-Inspired Spatial Patterning of ZIF-8 with Potential Applications in Optical Switch and Chemical Sensor. *ACS Appl. Mater. Interfaces* **9**, 38076–38080 (2017).

24. Wang, Y., Fedin, I., Zhang, H. & Talapin, D. V. Direct optical lithography of functional inorganic nanomaterials. *Science* **357**, 385–388 (2017).

25. Garcia, R., Knoll, A. W. & Riedo, E. Advanced scanning probe lithography. *Nat. Nanotechnol.* **9**, 577–587 (2014).

26. Kumar, R., Singh, N., Chang, C. K., Dong, L. & Wong, T. K. S. Deep-ultraviolet resist contamination for copper/low-k dual-damascene patterning. *J. Vac Sci. Technol. B* **22**, 1052 (2004).

27. Cheng, Y.-L., Lee, C.-Y. & Haung, C.-W. Plasma Damage on Low-k Dielectric Materials. *Plasma Science and Technology - Basic Fundamentals and Modern Applications* (2018).

28. Jung, Y. *et al.* Direct Photopatternable Organic–Inorganic Hybrid Materials as a Low Dielectric Constant Passivation Layer for Thin Film Transistor Liquid Crystal Displays. *J. Phys. Chem. C* **115**, 25056–25062 (2011).

29. Maldonado, J. R. & Peckerar, M. X-ray lithography: Some history, current status and future prospects. *Microelectron. Eng.* **161**, 87–93 (2016).

30. Chen, Y. Nanofabrication by electron beam lithography and its applications: A review. *Microelectron. Eng.* **135**, 57–72 (2015).

31. Gangnaik, A. S., Georgiev, Y. M. & Holmes, J. D. New Generation Electron Beam Resists: A Review. *Chem. Mater.* **29**, 1898–1917 (2017).

32. Park, K. S. *et al.* Exceptional chemical and thermal stability of zeolitic imidazolate frameworks. *Proc. Natl. Acad. Sci. U. S. A.* **103**, 10186–10191 (2006).

33. Banerjee, R. *et al.* High-Throughput Synthesis of Zeolitic Imidazolate Frameworks and Application to CO2 Capture. *Science* **319**, 939–943 (2008).

34. Widmer, R. N. *et al.* X-ray radiation-induced amorphization of metal–organic frameworks. *Phys. Chem. Chem. Phys.* **21**, 12389–12395 (2019).

35. Cruz, A. J. *et al.* Integrated Cleanroom Process for the Vapor-Phase Deposition of Large-Area Zeolitic Imidazolate Framework Thin Films. *Chem. Mater.* **31**, 9462–9471 (2019).

36. Innocenzi, P., Malfatti, L., Marmiroli, B. & Falcaro, P. Hard X-rays and soft-matter: processing of sol–gel films from a top down route. *J. Sol-Gel Sci. Technol.* **70**, 236–244 (2014).

37. E. Schweinefuß, M. *et al.* Zeolitic imidazolate framework-71 nanocrystals and a novel SOD-type polymorph: solution mediated phase transformations, phase selection via coordination modulation and a density functional theory derived energy landscape. *Dalton Trans.* **43**, 3528–3536 (2014).

38. Shen, K. *et al.* Ordered macro-microporous metal-organic framework single crystals. *Science* **359**, 206–210 (2018).

39. Sun, M.-H. *et al.* Applications of hierarchically structured porous materials from energy storage and conversion, catalysis, photocatalysis, adsorption, separation, and sensing to biomedicine. *Chem. Soc. Rev.* **45**, 3479–3563 (2016).
40. Luo, Y., Ahmad, M., Schug, A. & Tsotsalas, M. Rising Up: Hierarchical Metal–Organic Frameworks in Experiments and Simulations. *Adv. Mater.* **31**, 1901744 (2019).
41. Khay, I. *et al.* Assessment of the energetic performances of various ZIFs with SOD or RHO topology using high pressure water intrusion–extrusion experiments. *Dalton Trans.* **45**, 4392–4400 (2016).
42. Zhang, K. *et al.* Alcohol and water adsorption in zeolitic imidazolate frameworks. *Chem. Commun.* **49**, 3245–3247 (2013).
43. Dalstein, O. *et al.* Evaporation-Directed Crack-Patterning of Metal–Organic Framework Colloidal Films and Their Application as Photonic Sensors. *Angew. Chem. Int. Ed.* **56**, 14011–14015 (2017).
44. Teng, T. & Moffat, K. Primary radiation damage of protein crystals by an intense synchrotron X-ray beam. *J. Synchrotron Rad.* **7**, 313–317 (2000).
45. Saraev, V. V., Alsarsur, I. A., Annenkov, V. V. & Danilovtseva, E. N. Structure of Free Radicals Formed under X-ray Irradiation of Organic Polymeric Acids. *Rus. J. of Appl. Chem.* **74**, 1585–1589 (2001).
46. Choi, J. O., Moore, J. A., Corelli, J. C., Silverman, J. P. & Bakhru, H. Degradation of poly(methylmethacrylate) by deep ultraviolet, x-ray, electron beam, and proton beam irradiations. *J. Vac Sci. Technol. B* **6**, 2286–2289 (1988).
47. Zuber, G., Quada, J. C. & Hecht, S. M. Sequence Selective Cleavage of a DNA Octanucleotide by Chlorinated Bithiazoles and Bleomycins. *J. Am. Chem. Soc.* **120**, 9368–9369 (1998).
48. Yuan, R. *et al.* Chlorine-Radical-Mediated Photocatalytic Activation of C-H Bonds with Visible Light. *Angew. Chem. Int. Ed.* **52**, 1035–1039 (2013).
49. Lewandowski, M. & Ollis, D. F. Halide acid pretreatments of photocatalysts for oxidation of aromatic air contaminants: rate enhancement, rate inhibition, and a thermodynamic rationale. *J. Catal.* **217**, 38–46 (2003).
50. Sivaguru, P., Wang, Z., Zanoni, G. & Bi, X. Cleavage of carbon–carbon bonds by radical reactions. *Chem. Soc. Rev.* **48**, 2615–2656 (2019).
51. Luo, C. *et al.* Review of recent advances in inorganic photoresists. *RSC Adv.* **10**, 8385–8395 (2020).
52. Conrad, S. *et al.* Controlling Dissolution and Transformation of Zeolitic Imidazolate Frameworks by using Electron-Beam-Induced Amorphization. *Angew. Chem. Int. Ed.* **57**, 13592–13597 (2018).
53. Seo, E., Choi, B. K. & Kim, O. Determination of proximity effect parameters and the shape bias parameter in electron beam lithography. *Microelectron. Eng.* **53**, 305–308 (2000).
54. Rooks, M., Belic, N., Kratschmer, E. & Viswanathan, R. Experimental optimization of the electron-beam proximity effect forward scattering parameter. *J. Vac. Sci. Technol. B* **23**, 2769–2774 (2005).
55. Ocola, L. E. Nanoscale geometry assisted proximity effect correction for electron beam direct write nanolithography. *J. Vac. Sci. Technol. B* **27**, 2569–2571 (2009).
56. Li, K. *et al.* High speed e-beam writing for large area photonic nanostructures — a choice of parameters. *Sci. Rep.* **6**, 1–10 (2016).
57. Pérennès, F., De Bona, F. & Pantenburg, F. J. Deep X-ray lithography beamline at ELETTRA. *Nucl. Instrum. Meth. A* **467**–**468**, 1274–1278 (2001).
58. Amenitsch, H. *et al.* First performance assessment of the small-angle X-ray scattering beamline at ELETTRA. *J. Synchrotron Rad.* **5**, 506–508 (1998).
59. Hammersley, A. P., Svensson, S. O., Hanfland, M., Fitch, A. N. & Hausermann, D. Two-dimensional detector software: From real detector to idealised image or two-theta scan. *High Pressure Res.* **14**, 235–248 (1996).
60. Blessing, R. H. An empirical correction for absorption anisotropy. *Acta Cryst A* **51**, 33–38 (1995).
61. Sheldrick, G. M. A short history of SHELX. *Acta Cryst A* **64**, 112–122 (2008).
62. Spek, A. L. Single-crystal structure validation with the program PLATON. *J Appl Cryst* **36**, 7–13 (2003).

63. Spek, A. L. PLATON SQUEEZE: a tool for the calculation of the disordered solvent contribution to the calculated structure factors. *Acta Cryst C* **71**, 9–18 (2015).
64. Nečas, D. & Klapetek, P. Gwyddion: an open-source software for SPM data analysis. *Open Physics* **10**, 181–188 (2011).
65. Tu, M., Wannapaiboon, S., Khaletskaya, K. & Fischer, R. A. Engineering Zeolitic-Imidazolate Framework (ZIF) Thin Film Devices for Selective Detection of Volatile Organic Compounds. *Adv. Funct. Mater.* **25**, 4470–4479 (2015).
66. Herzinger, C. M., Johs, B., McGahan, W. A., Woollam, J. A. & Paulson, W. Ellipsometric determination of optical constants for silicon and thermally grown silicon dioxide via a multi-sample, multi-wavelength, multi-angle investigation. *J. Appl. Phys.* **83**, 3323–3336 (1998).